Sodium Hydride as a Powerful Reducing Agent for Topotactic Oxide Deintercalation: Synthesis and Characterization of the Nickel(I) Oxide $LaNiO_2$

M. A. Hayward, M. A. Green, M. J. Rosseinsky,* and J. Sloan

Contribution from the Inorganic Chemistry Laboratory, Department of Chemistry, University of Oxford, South Parks Road, Oxford OX1 3QR, U.K.

Received May 11, 1999

Abstract: The capability of sodium hydride as a reducing agent in oxide deintercalation reactions is explored. The Ni(III) perovskite $LaNiO_3$ can be reduced topotactically to $LaNiO_2$, isostructural with the "infinite layer" cuprates, using solid sodium hydride in a sealed evacuated tube at $190 \leq T/°C \leq 210$, and a similar infinite-layer phase is prepared by reduction of $NdNiO_3$. Structural characterization indicates the coexistence of incompletely reduced regions, with five-coordinate Ni centers due to the introduction of oxide anions between the NiO_2^{3-} sheets, giving samples with a refined stoichiometry of $LaNiO_{2.025(3)}$. Neutron powder diffraction and magnetization measurements indicate that the lamellar Ni(I) phase does not show the long-range antiferromagnetic ordering characteristic of isoelectronic Cu(II) oxides. This may be due either to the influence of the interlamellar oxide defect regions or to the reduced covalent mixing of Ni 3d and O 2p levels.

Introduction

Low-temperature synthesis is a developing area of solid-state chemistry, which allows access to metastable phases with novel electronic and chemical features.[1] Oxygen deintercalation from complex oxides is potentially an important aspect of this field, due to the widespread application of such phases arising from their electronic, magnetic, and catalytic properties. A variety of reduced oxides, particularly topotactically formed oxygen-deficient derivatives of the perovskite structure, have been reported.[2−8] The reagents employed to carry out these transformations have largely been hydrogen gas or finely divided electropositive metals, such as zirconium or aluminum, used as getters.[8,9] The reported reaction temperatures for these reductions lie above 300 °C, so there is clearly a need to develop reagents which are effective reducing agents at lower temperatures. This may then give access to metastable reduced oxides inaccessible, for thermodynamic reasons, at the higher temperatures required for hydrogen or getter reductions to proceed at acceptable rates. For example, the reduction of $LaNiO_3$ to $La_2Ni_2O_5$ with 5% H_2 diluted with N_2 requires a temperature of 390 °C, and the preparation of $La_2Ni_2O_5$ by the reduction of $LaNiO_3$ with a zirconium getter requires a temperature of at least 400 °C.[4]

In our present study, we have employed solid sodium hydride (NaH) as a novel reducing agent in the topotactic reduction of the Ni(III) perovskite oxide $LaNiO_3$ to the highly metastable Ni(I) phase $LaNiO_2$ and similar reduction of $NdNiO_3$ to form an analogous infinite-layer phase. This reaction is chosen as a suitable one to demonstrate the scope of NaH in this type of reduction chemistry because the Ni(I) phase has not been confirmed since the original report by Crespin et al.,[10,11] and other workers have made statements casting doubt on its existence.[12] The importance of this phase lies in the relation of its electronic properties to those of the isoelectronic d^9 Cu(II) parents of the cuprate superconductors, and the synthesis reported here allows us to determine the electronic properties of this phase.

The use of sodium hydride as a solid-state reductant follows the synthesis of both intermetallic hydrides[13] and amorphous precursors to ternary oxides with metal borohydrides in solution.[14−20] Metal hydrides are used extensively as drying and reducing agents in solution chemistry,[21] but their reducing power has been underexploited to this point in solid-state reactions.

(1) Stein, A.; Keller, S. W.; Mallouk, T. E. *Science* **1993**, *259*, 1558.
(2) Poeppelmeier, K. R.; Leonowicz, M. E.; Longo, J. M. *J. Solid State Chem.* **1982**, *45*, 71.
(3) Millange, F.; Caignaert, V.; Domenges, B.; Raveau, B.; Suard, E. *Chem. Mater.* **1998**, *10*, 1974.
(4) Alonso, J. A.; Martinez-Lope, M. J. *J. Chem. Soc., Dalton Trans.* **1995**, *17*, 2819−2824.
(5) James, M.; Attfield, J. P. *Physica C* **1994**, *235*, 751.
(6) Cava, R. J.; Takagi, H.; Krajewski, J. J.; Peck, W. F.; Hwang, H. Y. *Phys. Rev. B* **1993**, *47*, 11525.
(7) Hansteen, O. H.; Fjellvag, H.; Hauback, B. C. *J. Mater. Chem.* **1998**, *8*, 2089−2093.
(8) Hansteen, O. H.; Fjellvag, H.; Hauback, B. C. *J. Mater. Chem.* **1998**, *8*, 2081.
(9) Moriga, T.; Usaka, O.; Nakabayashi, I.; Kinouchi, T.; Kikkawa, S.; Kanamaru, F. *Solid State Ionics* **1995**, *79*, 252.
(10) Crespin, M.; Levitz, P.; Gatineau, L. *J. Chem. Soc., Faraday Trans. 2* **1983**, *79*, 1181.
(11) Crespin, M.; Levitz, P.; Gatineau, L. *J. Chem. Soc., Faraday Trans. 2* **1983**, *79*, 1195.
(12) Martinez-Lope, M. J.; Casais, M. T.; Alonso, J. A. *J. Alloys Compd.* **1998**, *277*, 109.
(13) Murphy, D. W.; Zahurak, S. M.; Vyas, B.; Thomas, M.; Badding, M. E.; Fang, W. C. *Chem. Mater.* **1993**, *5*, 767.
(14) Manthiram, A.; Dananjay, A.; Zhu, Y. T. *Chem. Mater.* **1994**, *6*, 1601−1602.
(15) Manthiram, A.; Tsang, C. *J. Electrochem. Soc.* **1996**, *143*, L143−L145.
(16) Tsang, C.; Kim, J.; Manthiram, A. *J. Solid State Chem.* **1998**, *137*, 28−32.
(17) Tsang, C.; Dananjay, A.; Kim, J.; Manthiram, A. *Inorg. Chem.* **1996**, *35*, 504−509.
(18) Tsang, C. F.; Manthiram, A. *J. Mater. Chem.* **1997**, *7*, 1003−1006.
(19) Tsang, C.; Lai, S. Y.; Manthiram, A. *Inorg. Chem.* **1997**, *36*, 2206−2210.
(20) Zhu, Y. T.; Manthiram, A. *J. Solid State Chem.* **1994**, *110*, 187−189.

10.1021/ja991573i CCC: $18.00
Published on Web 09/11/1999

Table 1. Products of the Reaction between $LaNiO_3$ and NaH As Observed by Powder X-ray Diffraction[a]

reaction conditions	temp/°C	reaction time	reaction products
ground	$T < 120$	2×1 week	no reaction
ground	$120 < T < 180$	4×3 days	reduction to $La_2Ni_2O_5$
ground	$180 < T < 210$	3×3 days	$LaNiO_2$, tetragonal phase ($a = 3.958$ Å, $c = 381$ Å) with anisotropically broad diffraction reflections
ground	$210 < T < 275$	2×3 days	reduction/disproportionation to $La_2Ni_2O_5 + Ni + La_2O_3$
ground	$275 < T$	1×3 days	reduction/disproportionation to $La_2NiO_4 + Ni$
separate	$T < 220$	2×3 days	no reaction
separate	$220 < T < 340$	1×3 days	reduction to $La_2Ni_2O_5$
separate	$340 < T$	1×3 days	reduction/disproportionation to $La_2Ni_2O_5 + Ni + La_2O_3$
annealed	$T < 210$	2×1 days	no change to diffraction pattern
annealed	$T < 210$	2×3 days	decomposition/disproportionation to $La_2Ni_2O_5 + Ni + La_2O_3$

[a] The outcome of the reactions with both ground and physically separated reagents are given, and the outcome of annealing the $LaNiO_{2+x}$ product in the absence of reducing agent is also presented.

The reduction potential of the H^-/H_2 couple has been estimated as -2.25 V,[22] making the hydride anion one of the most powerful reducing agents known. This thermodynamic driving force has allowed us to perform complex metal oxide reduction at lower temperatures than would be required for hydrogen gas or metal "getter" processes, enabling us to isolate the Ni^I phase, $LaNiO_2$, which has been reported to be unattainable by these two methods.[9,12]

$LaNiO_2$ was originally reported by Crespin et al. as a tetragonal phase observed during the hydrogen reduction of $LaNiO_3$ in a recirculating system.[10,11] An infinite-layer structure described by the stacking sequence $NiO_2^{3-}-La^{3+}-NiO_2^{3-}-La^{3+}$ was assigned to this phase, thus suggesting $LaNiO_2$ is both isoelectronic (Ni^I d^9) and isostructural with the Cu(II) parents of the high-T_c cuprate superconductors (e.g. $Ca_{0.85}Sr_{0.15}CuO_2$ [23]). The electronic properties of this reduced nickel oxide are of importance in the search to extend high-temperature superconductivity beyond copper, and so a reliable synthetic method for the synthesis of $LaNiO_2$ has been pursued by a number of workers.[12,24] In this paper we present details of the reduction chemistry of $LaNiO_3$ with the reducing agent NaH and a structural and magnetic characterization of the Ni^I phase, $LaNiO_2$. An analogous tetragonal $NdNiO_{2+x}$ phase is reported for the first time using the same synthetic method.

Powder neutron diffraction and high-resolution transmission electron microscopy show that the simple infinite-layer model for $LaNiO_2$ must be significantly modified by a novel defect structure consisting of additional oxide ions present in the space between the NiO_2^{3-} layers, producing both four-coordinate square-planar and five-coordinate square-pyramidal environments for nickel.

Experimental Section

Synthesis. Starting Materials. A 5 g amount of $LaNiO_3$ was synthesized via the coprecipitation of the metal ions from aqueous solution as described by Moriga et al.[9] An 8.82 g (2.03×10^{-2} mol) portion of $La(NO_3)_3 \cdot 6H_2O$ (Aldrich, 99.999%) and 5.93 g (2.03×10^{-2} mol) of $Ni(NO_3)_2 \cdot 6H_2O$ (Johnson-Matthey, 99.9985%) were dissolved in separate aliquots of 100 mL of distilled water to make solutions with concentrations of approximately 0.203 mol L^{-1}. The exact metal ion concentrations were determined by inductively coupled plasma emission spectroscopy (to account for variable levels of hydration in the starting materials), and the two solutions were then combined such that a 1:1 molar ratio of La to Ni was achieved. The metal ions were precipitated from the resulting solution with tetramethylammonium hydroxide (Aldrich, 25 wt % solution in H_2O) to form an intimately mixed hydroxide sol. This green precipitate was immediately filtered and washed with copious amounts of distilled water and then ethanol. The resulting green jelly was heated on a hot plate to 200 °C to decompose the organic coprecipitating agent. The black decomposition product was finely ground and then treated in one of two ways. "Ambient pressure" $LaNiO_3$ was synthesized by pressing the decomposition product into 13 mm diameter pellets at 5 tons of pressure and then firing at 850 °C under 1 atm of flowing oxygen for two periods of 30 h with one intermediate regrinding. "High pressure" $LaNiO_3$ was synthesized by pressing the decomposition product into 7 mm pellets, which were then wrapped in gold foil and heated for two periods of 24 h at 1000 °C under a static pressure of 200 atm of oxygen in a manner similar to that described by Alonso et al.[4] The high-pressure apparatus used in this synthesis employs a compressor to pressurize a sealed vessel, made from Rene-41 alloy, which is then heated to the reaction temperature by an external furnace. The products of both synthetic methods were analyzed by powder X-ray diffraction and found to be in good agreement with previously published patterns.[25]

$NdNiO_3$ was synthesized in a manner similar to that described for "high pressure" $LaNiO_3$. Intimately mixed Nd/Ni hydroxide sols were decomposed at 200 °C in air, pressed into 7 mm pellets, and heated for two periods of 24 h at 1000 °C under a pressure of 200 atm of oxygen as described above. Powder X-ray diffraction patterns showed the product to be monophasic and yielded lattice parameters in good agreement with previously published values for orthorhombic $NdNiO_3$.[26]

Reduction of $LaNiO_3$ with NaH. The reduction of $LaNiO_3$ was performed using NaH as a reducing agent. A double stoichiometric excess of NaH (Aldrich 95%, NaOH was the only impurity observable by X-ray diffraction) was ground with $LaNiO_3$ (typically 100 mg (4.16 mmol) of NaH with 500 mg (2.04 mmol) of $LaNiO_3$), in a He-filled Mbraun Labmaster drybox and then sealed in an evacuated Pyrex ampule ($p < 2 \times 10^{-4}$ Torr). The sealed reaction vessels were then heated under conditions described in Table 1, to fully explore the reducing behavior of the reagents. The reaction progress was monitored via powder X-ray diffraction from well-ground reaction products, loaded into O-ring-sealed sample holders in the drybox, and measured on a Philips PW1710 diffractometer. When the X-ray data showed that the reaction had reached completion, the products were then washed with CH_3OH to remove the NaOH (produced as a reaction byproduct) and any unreacted NaH from the reaction mixture. Typically, 5×60 mL of CH_3OH (which had been previously dried by distillation from Mg) were transferred via cannula onto 500 mg of reaction products in a 100 mL filter Schlenk, under a nitrogen atmosphere. The suspension was then vigorously agitated, for one minute, to allow the sodium phases to react/dissolve before being filtered. After filtration the samples were dried under vacuum for 2 h. The complete removal of the sodium phases

(21) Harwood, L. M.; Moody, C. J. *Experimental Organic Chemistry − Principles and Practice*; Blackwell Scientific: Oxford, U.K., 1989.
(22) Cotton, F.; Wilkinson, G. *Inorganic Chemistry*, 4th ed.; Wiley-Interscience: New York, 1980; p 249.
(23) Siegrist, T.; Zahurak, S. M.; Murphy, D. W.; Roth, R. S. *Nature* **1988**, *334*, 231.
(24) Moriga, T.; Usaka, O.; Nakabayashi, I.; Hirashima, Y.; Kohno, T.; Kikkawa, S.; Kanamaru, F. *Solid State Ionics* **1994**, *74*, 211−217.
(25) Garcia-Munoz, J. L.; Rodriguez-Carvajal, J.; Lacorre, P.; Torrance, J. B. *Phys. Rev. B* **1992**, *46*, 4414−4425.
(26) Demazeau, G.; Marbeuf, A.; Pouchard, M.; Hagenmuller, P. *J. Solid State Chem.* **1971**, *3*, 582.

was then confirmed by X-ray powder diffraction and the chemical techniques outlined below.

Bulk powder samples suitable for powder neutron diffraction experiments were prepared by reacting 5 g (2.03×10^{-2} mol) of "ambient pressure" $LaNiO_3$ with 980 mg (4.08×10^{-2} mol) of NaH at 190 °C, as described above, for five periods of 3 days with regrinding between each heating period.

To investigate the role of solid−solid versus solid−gas reactions in the mechanism by which NaH reduces $LaNiO_3$, reductions were performed by loading $LaNiO_3$ (500 mg, 2.04 mmol) and NaH (100 mg, 4.16 mmol) into separate clean Pyrex "thimbles", under a helium atmosphere, which were then loaded and sealed under vacuum in a larger Pyrex vessel, such that the two reagents experienced the same atmosphere inside the larger vessel but were not in physical contact.

Reduction reactions were also performed using ground mixtures of $NdNiO_3$ (500 mg, 1.99 mmol) and NaH (100 mg, 4.16 mmol) in the temperature range $160 < T/°C < 210$.

Characterization. Compositional Characterization. EDX analysis was performed on a large number of crystallites, using a JEM-2010 microscope fitted with a windowless Si(Li) detector and operated using the LINK "pentafet" energy-dispersive X-ray (EDX) microanalysis system, to ensure no residual sodium remained in the samples.

Thermogravimetric and differential scanning calorimetry measurements were performed using a Rheometric Scientific STA 1500 thermal analyzer. Samples of around 50 mg were loaded rapidly into platinum crucibles and then heated at 4 °C min^{-1} under flowing oxygen.

Structural Characterization. Neutron powder diffraction data were collected on 5 g samples (which were indium-sealed in vanadium cans under helium) on the D1B instrument at 5 and 290 K and on the D2B instrument at 298 K at the Institut Laue Langevin, Grenoble, France. Rietveld profile refinement was performed, on the neutron powder diffraction data collected from the material, using the GSAS suite of programs[27] employing a pseudo-Voigt peak shape and a 16-term cosine Fourier series background function.

The DIFFaX program[28,29] was employed to simulate the effect of stacking faults and intergrown defect layers on powder diffraction patterns. Models were described by the stacking of defined layers according to the transition probability α_{ij} (the probability of layer j being stacked on top of layer i) and the translation vector $\mathbf{R}_{ij}$ (the vector between the origin of layer i and layer j, described as a fraction of the basis unit cell vectors).

High-resolution transmission electron microscopy (HRTEM) measurements were performed using a JEOL 4000EX microscope operating at 400 kV (point resolution ca. 1.7 Å). Finely ground samples were dispersed ultrasonically in methanol, under N_2, and then placed dropwise onto lacy carbon grids (Agar, Cu 300 mesh) which were rapidly inserted into the microscope to avoid oxidation by the air. The electron diffraction patterns collected were indexed and *d* spacings calculated, using a camera length obtained from a reference TlCl standard pattern, with an estimated accuracy of ±0.05 Å. High-resolution lattice images were recorded close to the ideal Scherzer defocus. Simulations of these images were calculated using the EMS suite of programs.[30] Fourier transforms of selected areas of recorded lattice images were calculated using the Scion image program.[31]

Magnetic and Electronic Characterization. Magnetic data were collected, on samples contained within sealed gelatin capsules (which had been previously loaded in the drybox), using a Quantum Design MPMS SQUID magnetometer.

All samples were found to be contaminated by small (1.5−5 mass %) quantities of ferromagnetic impurity assigned as nickel metal. The paramagnetic susceptibility of the bulk $LaNiO_2$ material was measured by saturating the ferromagnetic part of the signal (in fields larger than 3 T) and then measuring magnetization-field isotherms. The paramagnetic susceptibility of the sample was taken to be the slope of the linear high-field sections of these plots. A simple subtraction of two high-field magnetization measurements ($H > 3$ T) proved insufficiently precise due to the small (∼10% in 4 T) contribution of the paramagnetic component to the sample magnetization. To this end a sample of $LaNiO_2$ (63 mg) prepared from high-pressure $LaNiO_3$ was selected, as displaying minimal ferromagnetic contamination (∼1.6% by mass), and cooled in a 3 T field to 6 K. The magnetization of the sample was measured in 10 fields up to 5 T. This procedure was repeated at 52 temperatures from 6 to 300 K. The magnetization-field isotherms were fitted to a linear function, with data points with large errors being excluded from the fit. All fits had at least seven points.

An estimate of the resistivity of samples was measured by pressing a small amount of the sample in question (about 200 mg) between two brass pistons, within a Perspex tube of diameter 4 mm. In an attempt to minimize undesirable contact effects, the two pistons were forced together by means of an electrically insulated clamp, compressing the sample and ensuring good electrical contact between all components. The electrical resistance between the two pistons was measured, thus allowing an estimate of the resistivity of the sample to be calculated. The whole procedure was performed under an argon atmosphere to prevent oxidation of samples by the air.

Results

Dependence of Reaction Products on Synthetic Conditions. The outcome of the reaction between $LaNiO_3$ and NaH is critically dependent on the synthetic conditions, as summarized in Table 1. The reactions between ground mixtures of $LaNiO_3$ and NaH show an evolution of reducing power and reaction pathway with temperature. In the lowest temperature range ($120 < T/°C < 180$) mixtures of $LaNiO_3$ and NaH yield the monoclinic phase $La_2Ni_2O_5$.[4]

Elevation of the temperature into the range $180 < T/°C < 210$ yields a tetragonal phase ($a = 3.958$ Å, $c = 3.381$ Å, $V = 52.96$ Å^3). This is assigned as $LaNiO_2$ by comparison of the lattice parameters with the only previous report of this Ni(I) phase[11] ($a = 3.966$ Å, $c = 3.376$ Å, $V = 53.10$ Å^3). Powder X-ray diffraction measurements following the evolution of the reduction with time at 190 °C are shown in Figure 1 (a 1:1 ratio of $LaNiO_3$ to NaH was used in this reaction to reduce the reaction rate and allow the observation of intermediate phases). These data show that tetragonal $LaNiO_2$ is formed via the monoclinic Ni(II) phase $La_2Ni_2O_5$. Direct reduction of $La_2Ni_2O_5$ with NaH in the temperature range $180 < T/°C < 210$ results in the synthesis of the same tetragonal phase. In order for the reduction of $LaNiO_3$ to $LaNiO_2$ to approach completion, a 2:1 stoichiometric excess of NaH and repeated regrinding is required, particularly for large samples (5 g samples prepared for neutron diffraction experiments required 5×3 days to reach completion, as opposed to 500 mg samples, which required 3×3 days).

At temperatures within the range $210 < T/°C < 275$, disproportionation to $La_2Ni_2O_5$, La_2O_3, and Ni follows the reduction to Ni(I). Increasing the temperature to $275 < T/°C < 300$ induces a different disproportionation route, to La_2NiO_4 and Ni. At higher temperatures, the presence of NaOH yields a mixture of lanthanum hydroxides and oxyhydroxides and nickel metal.

The reduction reactions performed with physically separated reagents follow a different scheme. Below 220 °C there is no observable reduction of $LaNiO_3$. In the range $220 < T/°C < 340$ $LaNiO_3$ is reduced to $La_2Ni_2O_5$. Above 340 °C disproportionation produces mixtures of $La_2Ni_2O_5$, La_2O_3, and Ni, which become completely reduced to La_2O_3 and Ni as the temperature approaches 400 °C.

(27) Larson, A. C.; Von Dreele, R. B. *General Structural Analysis Systems*; Los Alamos National Laboratory: Los Alamos, NM, 1994.

(28) Treacy, M. M. J.; Newsam, J. M.; Deem, M. W. *Proc. R. Soc. London, Ser. A* **1991**, *433*, 499.

(29) Treacy, M. M. J.; Deem, M. W. Diffax − A Computer Program for the Calculating of Diffraction Intensity from Faulted Crystals, version 1.765, 1991.

(30) Stadelmann, P. A. *Ultramicroscopy* **1987**, *21*, 131.

(31) Rasband, W. Scion image; Scion Corp., 1998.

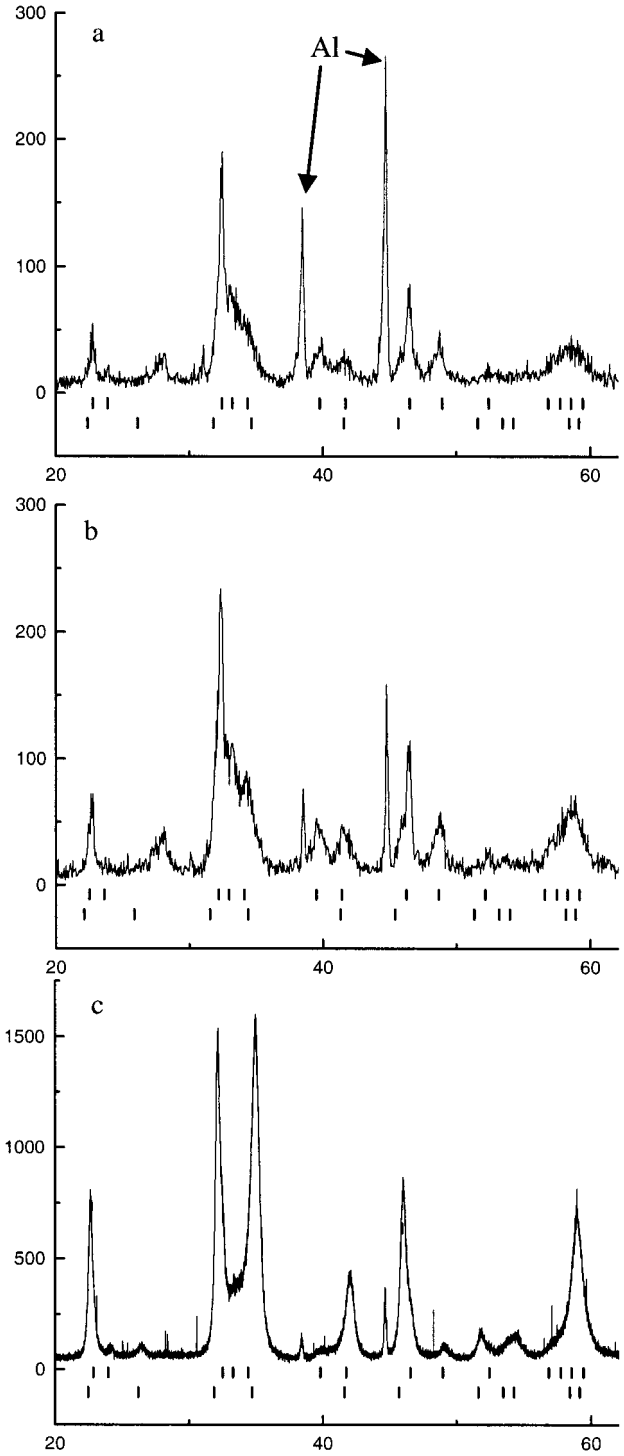

Figure 1. Evolution of the powder X-ray diffraction pattern, with time, of a 1:1 molar mixture of intimately ground $LaNiO_3$ and NaH at 190 °C: (a) after 24 h, the sample is mainly $La_2Ni_2O_5$; (b) after 36 h, reflections due to $LaNiO_2$ are appearing; (c) after 48 h, the sample is mainly $LaNiO_2$ but with traces of $La_2Ni_2O_5$. The upper tick marks correspond to the positions of the most intense peaks of $La_2Ni_2O_5$ and the lower marks to those of $LaNiO_2$. Sharp reflections at ~38 and 44° are due to the aluminum sample holder.

The success of the CH_3OH washing process at removing the sodium-containing phases was demonstrated by elemental analysis, X-ray diffraction, and EDX. No signals due to the presence of sodium could be observed by either technique. Figure 2 shows the powder X-ray diffraction patterns of the tetragonal phase, assigned as $LaNiO_2$, (a) before and (b) after washing with CH_3OH. Figure 2c shows a typical EDX spectrum

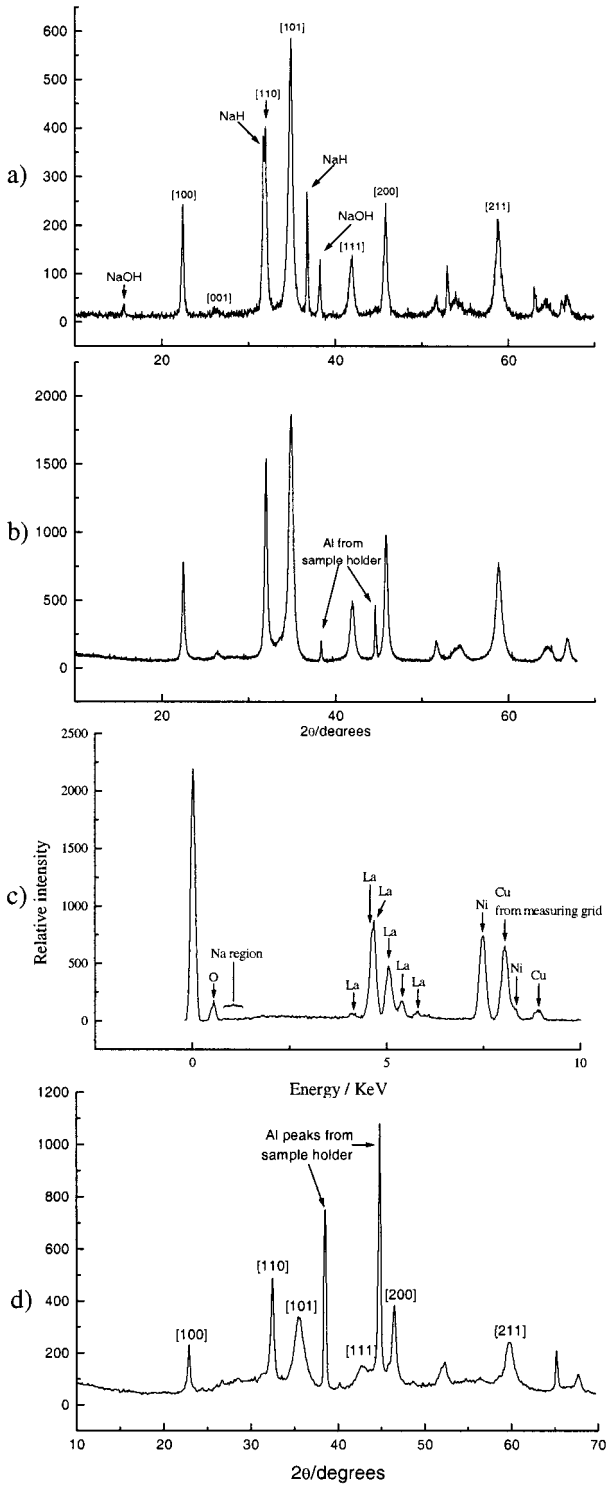

Figure 2. (a) X-ray powder diffraction pattern of products of the reaction between $LaNiO_3$ and NaH after three periods of 3 days at 190 °C. Bragg reflections are indexed according to the tetragonal cell of infinite layer $LaNiO_2$, and peaks due to NaH and NaOH are marked. (b) X-ray powder diffraction pattern of reaction products for (a) after washing with CH_3OH under nitrogen. (c) EDX spectrum of the washed reaction products. No peaks due to sodium are observed, demonstrating the complete removal of the sodium-containing phases. (d) X-ray powder diffraction pattern of the infinite-layer $NdNiO_{2+x}$ phase, after washing with CH_3OH to remove sodium-containing phases. Note the greater peak width anisotropy than is observed in $LaNiO_{2+x}$ phases.

of the washed product, confirming complete removal of the sodium-containing phases.

Annealing of washed $LaNiO_2$ samples, in sealed evacuated

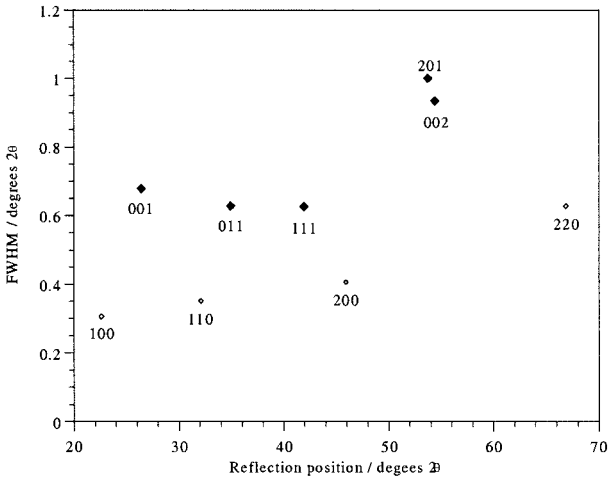

Figure 3. Angular variation (2θ/deg) of the full width at half-maximum height of X-ray powder diffraction reflections of $LaNiO_2$ reduced from ambient-pressure $LaNiO_3$ (open symbols mark diffraction reflection of the class $\langle hk0\rangle$ and closed symbols those of the class $\langle h,k,l\neq 0\rangle$).

Pyrex ampules, at temperatures below 210 °C resulted in no observable change to the X-ray powder diffraction patterns of these samples. Annealing at temperatures greater that 210 °C resulted in slow but significant broadening of all reflections and, on raising the temperature above 300 °C, a more rapid decomposition to $La_2Ni_2O_5$, La_2O_3, and Ni. $LaNiO_2$ is not stable with respect to disproportionation above 210 °C.

Magnetic measurements described above indicate the presence of 1.5−5% nickel metal impurities by mass, in $LaNiO_{2+x}$ samples. The exact amount present is heavily dependent on the quality of the $LaNiO_3$ starting material and is smallest in the case of "high pressure" $LaNiO_3$.

All chemical manipulations of $LaNiO_{2+x}$ phases were performed so as to exclude atmospheric oxygen and water. Monitoring of $LaNiO_2$ samples exposed to air over time, via X-ray powder diffraction, reveals that all Bragg reflections start to broaden after 20 min, with samples becoming almost entirely amorphous after 4 h at room temperature. At elevated temperatures (above 100 °C) reoxidation to poorly crystalline $LaNiO_3$ occurs in less than 1 h.

Preparation of $NdNiO_{2+x}$. The reduction of $NdNiO_3$ with NaH appears to occur at temperatures lower than those for $LaNiO_3$. No reaction was observed below 160 °C, but in the range $160 < T/°C < 200$ a tetragonal phase ($a = 3.9251(9)$ Å, $c = 3.323(1)$ Å, $V = 51.195$ Å^3) was formed. A powder X-ray diffraction pattern of this phase, after washing with CH_3OH, is shown in Figure 2d. By analogy with $LaNiO_2$ this phase was assigned as $NdNiO_{2+x}$. Above 200 °C largely amorphous reaction products were produced. The only crystalline phase which could be identified in any of these patterns was Nd_2O_3. No intermediate phase, analogous to $La_2Ni_2O_5$, was observed during reactions, even at low temperatures. The reduction proceeds directly to the tetragonal phase described above with no crystalline intermediates.

Structural Analysis and Refinement of $LaNiO_2$. The diffraction patterns of this tetragonal phase, collected from all the samples synthesized within the temperature range $180 < T/°C < 210$, display highly anisotropic peak widths, as shown in Figure 3. The sharper reflections are those from diffraction planes of the class $\langle hk0\rangle$, and the broad peaks are from the class where l has a nonzero value, characteristic of anisotropic particle size, stacking disorder, or uniaxial strain in layered compounds, as has been observed in a number of other topotactically reduced oxides.[32]

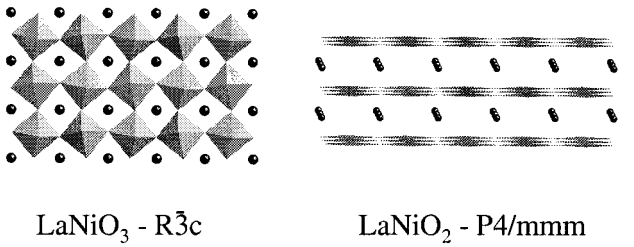

Figure 4. Relation between the rhombohedral structure of $LaNiO_3$ and the infinite-layer model proposed for $LaNiO_2$[10,11] viewed along [100]. The stacking axis of $LaNiO_2$ is vertical in this representation.

Attempts to reduce the observed peak width anisotropy by varying the synthetic conditions proved unsuccessful. The temperature range over which this tetragonal phase can be synthesized is very small, as described in Table 1, and varying the reaction or annealing temperature within this small window did not alter the peak width anisotropy.

Reduction of more crystalline $LaNiO_3$ prepared under high oxygen pressure (the fwhm of the 110 reflection was 15% smaller than for "ambient pressure" $LaNiO_3$) gave an $LaNiO_{2+x}$ product with narrower Bragg reflections (fwhm reduced by ∼30%). However, the highly anisotropic diffraction peak widths observed in all previous samples were still as marked.

Structural Refinement. Rietveld profile refinement was performed, in the space group *P*4/*mmm*, on neutron powder diffraction data collected for $LaNiO_2$. The starting point for these refinements was the model proposed by Crespin et al., which consists of infinite NiO_2 layers, separated by eight-coordinate La^{3+} ions. $LaNiO_3$ is a rhombohedrally distorted cubic perovskite,[25] but it can be converted to an infinite-layer structure by the ordered removal of one-third of the oxide ions (Figure 4).

The large peak width anisotropy was modeled with anisotropic size and strain broadening parallel and perpendicular to the [001] axis, producing significant improvement to all "goodness of fit" parameters. Ferromagnetically ordered nickel metal was inserted into the refinement as a second phase.

The fit to the data, using a model with a single tetragonal lanthanum nickelate phase, is unsatisfactory ($\chi^2 = 3.222$). Electron diffraction patterns obtained from the sample can be readily assigned to the [001], [0−11], and [−111] zone axes in the *P*4/*mmm* space group (Figure 5) and display no supercell reflections and, thus, unambiguously confirm the space group assignment. This suggests that the discrepancies between the structural model and the observed data are due to microstructural effects within the sample, which do not lead to a lowering of symmetry.

The simulation of the [001] zone lattice image (Figure 5d), using the simple infinite-layer model, is in good agreement with the observed projected potential at the calculated defocus, implying that defects along the interlamellar axis are an important component of the correct structural model.

Figure 6 shows a lattice image of the [100] zone axis of a different crystallite of $LaNiO_2$ where a defect region (b) within the bulk structure (a) is apparent. The nature of this defect region is revealed by the calculated electron diffraction patterns obtained by Fourier transformation of the images of these two areas. The inset (c) is the calculated diffraction pattern of the ordered region (a), which can be readily indexed as the [100] zone axis of a primitive tetragonal cell with lattice parameters in a ratio consistent with those obtained for $LaNiO_2$ from the

(32) Retoux, R.; Rodriguez-Carvajal, J.; Lacorre, P. *J. Solid State Chem.* **1998**, *140*, 307.

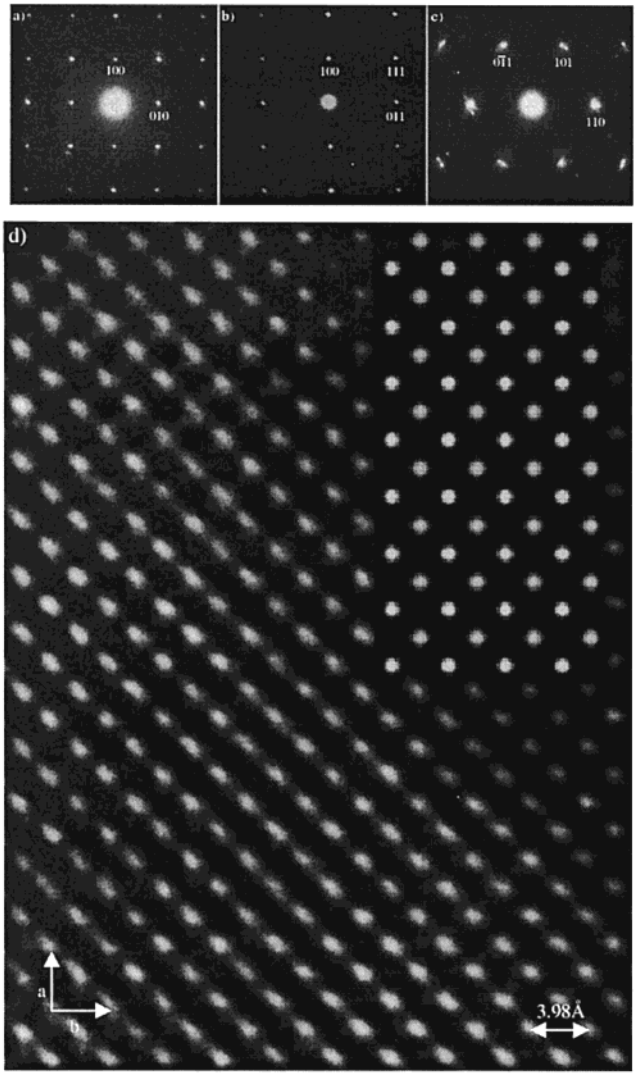

Figure 5. Electron diffraction patterns of the (a) [001], (b) [0−11], and (c) [−111] zone axes of $LaNiO_2$ indexed in the space group *P*4/*mmm*. (d) Lattice image of the [001] zone axis of $LaNiO_2$, including inset (top right) simulated, within the EMS suite of programs,[30] using the infinite-layer model and employing the following microscope parameters: accelerating voltage, 400 kV; spherical aberration coefficient, 0.9 nm; semi-convergence angle, 0.8 mrad; objective lens aperture, 10 nm.

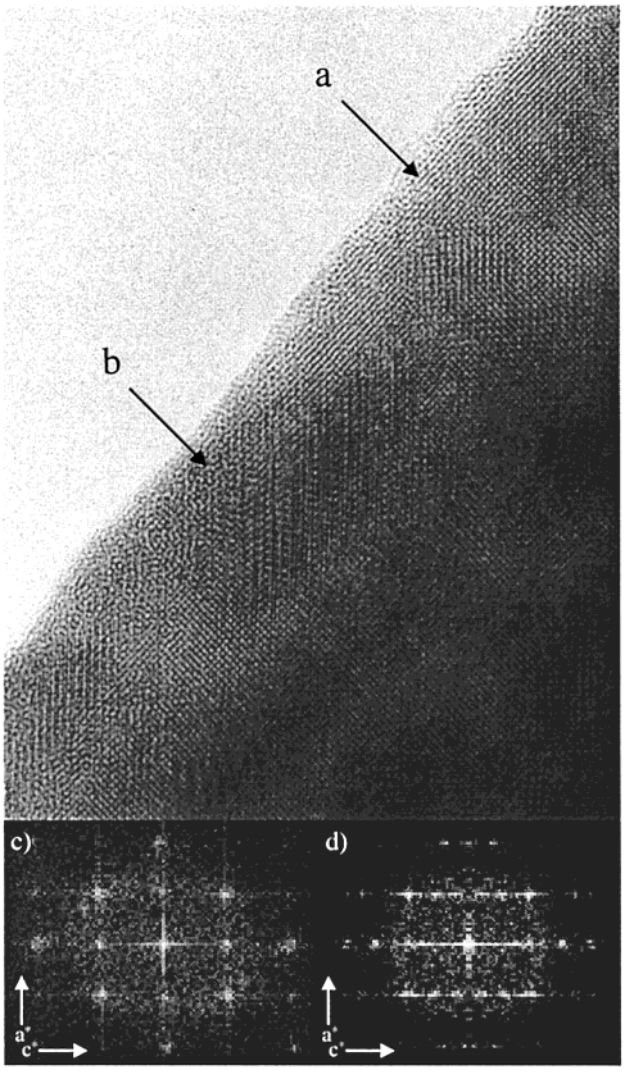

Figure 6. Lattice image of the [100] zone axis of $LaNiO_2$ showing ordered (a) and disordered domains (b) and Fourier transforms of the respective regions (c, d). The Fourier transforms correspond to the electron diffraction patterns of these region and are indexed according to the reciprocal space of tetragonal $LaNiO_2$.

bulk neutron diffraction data. The inset (d) is the calculated diffraction pattern from the defect region (b), which also displays a tetragonal motif with an *a* lattice parameter consistent with $LaNiO_2$. However, the *c** direction exhibits extensive streaking, indicating extensive strain or structural disorder parallel to the [001] axis. The occurrence of such highly disordered or strained domains may be correlated with the poor Rietveld fit with the simple infinite-layer model and suggests that the powder diffraction data might be more effectively modeled by introducing a second tetragonal lanthanum nickelate phase to account for these regions of the sample.

By combination of multiple-phase Rietveld refinement techniques with the DIFFaX simulation program, an investigation into possible defects present in the sample was performed. A second tetragonal lanthanum nickelate phase was added to the Rietveld profile refinement, with atomic coordinates identical with those of the first phase, and freely refined lattice parameters, Lorentzian peak profile coefficients, and thermal parameters. The Gaussian profile width was constrained to be the same as in the other phases, to model the instrumental contribution to the profile. This led to a marked improvement in the fit quality ($\chi^2 = 2.16$).

The atomic displacement parameters of the nickel and oxygen atoms in the second phase were significantly larger than those of the lanthanum ($U_{Ni} = 0.106$ Å^2, $U_O = 0.051$ Å^2, $U_{La} = 0.0064$ Å^2) and than those of all the atoms in the majority $LaNiO_2$ phase ($U_{Ni} = 0.0051$ Å^2, $U_O = 0.0089$ Å^2, $U_{La} = 0.0010$ Å^2), consistent with the increased disorder observed in the lattice image (Figure 6b). Components of the anisotropic displacement ellipsoids were markedly anisotropic, with displacement parallel to the *c* axis nearly 7 times greater than those in the *ab* plane. This, together with the expansion along the stacking direction of the minority phase ($a_{maj} = 3.959$ Å, $c_{maj} = 3.374$ Å, $a_{min} = 3.943$ Å, $c_{min} = 3.454$ Å), suggests displacive disorder of the NiO_2 sheets along the stacking direction produced by an interlamellar defect of residual oxide anions at the (0, 0, $^1/_2$) position. The close contacts from this defect anion to the layers led to each interlamellar anion displacing the two adjacent NiO_2 layers; therefore, additional nickel and oxygen atoms were inserted into the second phase at (0, 0, *z*) and ($^1/_2$, 0, *z*′), respectively, to model this, with the occupancies of sites constrained such that the stoichiometry of the NiO_2^{3-} layers and the La/Ni ratio were maintained (relaxation of these

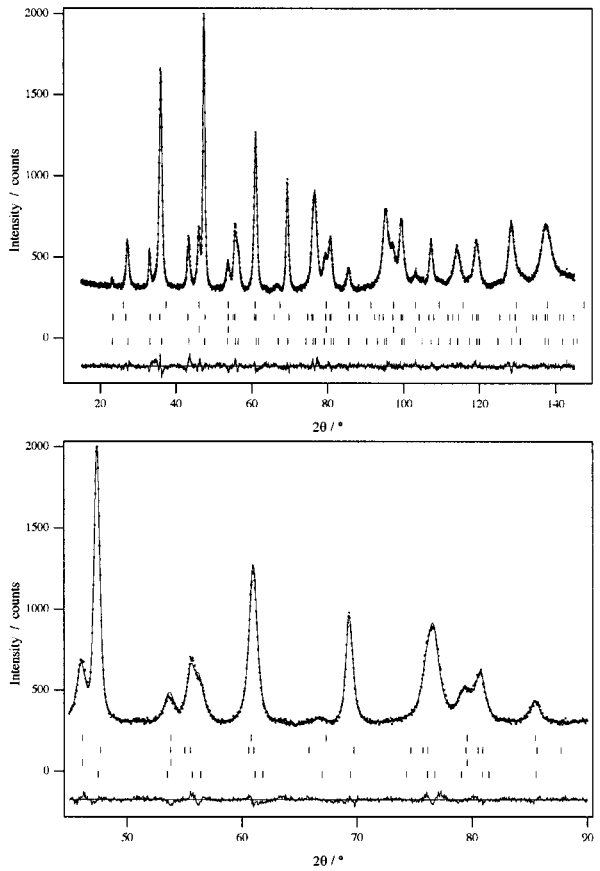

Figure 7. Observed, calculated, and difference plots for the final Rietveld refinement of $LaNiO_2$, from powder neutron diffraction data, employing a two-phase model and disordered displacements in the minority phase. The expanded region $45 < 2\theta/\text{deg} < 90$ shows the improvement to the fit achieved by the insertion of a second disordered phase in comparison with Figure S1 (Supporting Information).

constraints did not result in a change in the refined stoichiometry of greater than 2%). The ($^1/_2$, 0, 0) in-plane oxide anion was refined to be fully occupied.

This modification of the model gave a χ^2 value of 1.89 and a physically reasonable explanation of the anisotropic broadening which dominates the observed diffraction pattern. Finally, to relax the rather short bond length between the lanthanum position ($^1/_2$, $^1/_2$, $^1/_2$) and the disordered oxygen at ($^1/_2$, 0, z) (2.21 Å) in the minority phase the lanthanum site was split by the introduction of a second site at a ($^1/_2$, $^1/_2$, z) position with an occupancy constrained in the same manner as the nickel disorder site, giving a final χ^2 value of 1.881 and a relaxed La−O bond length of 2.38 Å.

The observed, calculated, and difference plots for the final Rietveld refinement of $LaNiO_{2.03}$ are shown in Figure 7, with structural data and goodness of fit parameters listed in Table 2. Refined bond lengths and ORTEP diagrams of the two refined phases are shown in Figure 8, with bond lengths and angles for the minority phase shown in Table 2. The respective peak broadening contributions from particle size and structural strain in the two phases are detailed in Table S1 of the Supporting Information. [35]

Table 2. Structural Data for the Final Rietveld Refinement of $LaNiO_2$ Refined from Neutron Powder Diffraction Data[a]

Phase 1: Space Group *P*4/*mmm*

	x	*y*	*z*	U_{iso}/Å^2	site sym
Ni	0	0	0	0.00026(6)	1 a 4/*mmm*
La	0.5	0.5	0.5	0.00040(3)	1 d 4/*mmm*
O	0.5	0	0	0.0032(8)	2 f *mmm*

$a = 3.9592(1)$ Å, $c = 3.3745(2)$ Å; mole fraction 59.30(3)%

Phase 2: Space Group *P*4/*mmm*

	x	*y*	*z*	fraction	U_{iso}/Å^2	site sym
Ni_1	0	0	0	0.639(43)	0.081(7)	1 a 4/*mmm*
Ni_2	0	0	0.211(10)	0.180(21)	0.027(7)	2 g 4*mm*
La_1	0.5	0.5	0.5	0.639(43)	0.0058(2)	1 d 4/*mmm*
La_2	0.5	0.5	0.601(17)	0.180(21)	0.0087(1)	2 h 4*mm*
O_1	0.5	0	0	0.639(43)	0.061(6)	2 f *mmm*
O_2	0.5	0	0.210(15)	0.180(21)	0.033(4)	4 i 2*mm*
O_3	0	0	0.5	0.090(11)	0.083(6)	1 b 4/*mmm*

$a = 3.9431(8)$ Å, $c = 3.454(2)$ Å; mole fraction 23.7(2)%

Ni Metal Phase: Space Group F$m\bar{3}m$

	x	*y*	*z*	U_{iso}/Å^2	site sym
Ni	0	0	0	0.0011(6)	4 a $m\bar{3}m$

$a = 3.5229(3)$ Å magnetic moment $= 0.568\ \mu_B$ mole fraction: 16.7(2)%

Goodnesss of Fit Parameters

R_{wp}	2.94%
R_p	2.27%
χ^2	1.881

bond	dist/Å	bond	dist/Å
Ni_1-O_1	1.9716(4)	La_2-O_1	2.4075(6)
Ni_2-O_2	1.9716(4)	La_2-O_2	2.388(30)
Ni_2-O_3	2.46(4)	La_1-Ni_1	3.2798(7)
La_1-O_1	2.6210(7)	La_1-Ni_2	3.715(30)
La_1-O_2	3.15(4)	La_2-Ni_1	3.111(6)
La_1-O_3	2.7882(6)	La_2-Ni_2	3.095(15)
bond	angle/deg	bond	angle/deg
$O_2-Ni_2-O_2$	179.764(11)	$O_2-Ni_2-O_3$	89.9(13)

[a] Phase 1 is the majority "perfect" infinite-layer phase representing regions of the sample which have the stoichiometry $LaNiO_2$. Phase 2 represents defective regions of the sample which have interlamellar oxide ion defects which change the stoichiometry of the phase to $LaNiO_{2.09}$. Refined bond lengths and angles refer to atom labels for phase 2 shown in Figure 8b.

The disordered minority phase, shown in Figure 8b, can be described as a superposition, or intergrowth, of two different stacking sequences (labeled I and II) and is depicted more clearly in Figure 9a. Special attention should be drawn to the lanthanum disorder site (La_2) and the large displacement parameters of the Ni_1 and O_1 atoms in this minority phase. These features can be correlated with the relaxation of what would otherwise be short La−O bond lengths in the $NiO_2-La-NiO_2-La$ matrix around a defect $NiO_2-LaO-NiO_2$ layer, as shown in Figure 9a.

The validity of this defect model can be tested, and extra information about the correlation between defect locations gained, by simulating powder diffraction patterns of this disordered intergrowth using the DIFFaX simulation program. The program employs a recursion algorithm to calculate kinematical diffraction intensities for crystals containing planar faults.[28,29]

A faulted crystal, corresponding to intermingled stacking of $LaNiO_2$ infinite layers and $LaNiO_{2+x}$ defect layers, constrained by the refined stoichiometry, can be constructed as shown in Figure 10 by defining the probabilities of transitions between the block types, relative to defined unit cell parameters, as described in Table 3. Layer 1 corresponds to the "perfect" stoichiometric $LaNiO_2$ majority phase refined from the neutron powder diffraction data. Layers 2 and 3 represent the two

(33) Greenwood, N. N.; Earnshaw, A. *Chemistry of the Elements*, 2nd ed.; Butterworth-Heinemann: Oxford, U.K., 1997; p 1149.

(34) Chrzan, D. C.; Falicov, L. M.; Maclaren, J. M.; Zhang, X. G.; Gonis, A. *Phys. Rev. B* **1991**, *43*, 9442.

(35) Larson, A. C.; Von Dreele, R. B. *GSAS Technical Manual*; Los Alamos National Laboratory: Los Alamos, NM, 1994.

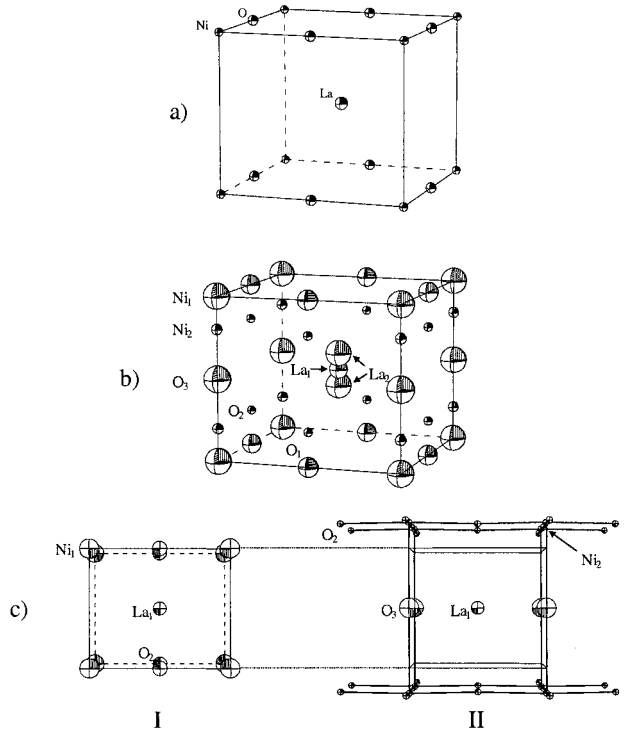

Figure 8. (a) ORTEP plot and bond lengths for majority infinite-layer phase $LaNiO_2$. Atoms are represented as ellipsoids of 100 times the refined value. The Ni^{+} and La^{3+} cations are in square and square-prismatic coordinations, respectively, with refined bond lengths of Ni−O = 4 × 1.979 60(6) Å and La−O = 8 × 2.6010(1) Å. (b) ORTEP plot for the minority defect $LaNiO_{2+x}$ phase found to be in the $LaNiO_2$ sample. (c) Representation of (b) as the superposition of an infinite-layer phase (I) and a defect phase with interlamellar oxygen ions (II), and the consequent relaxation of the atomic positions around the defect. The La_2 position is required to relax the short La−O distances at the interface between defect and bulk regions.

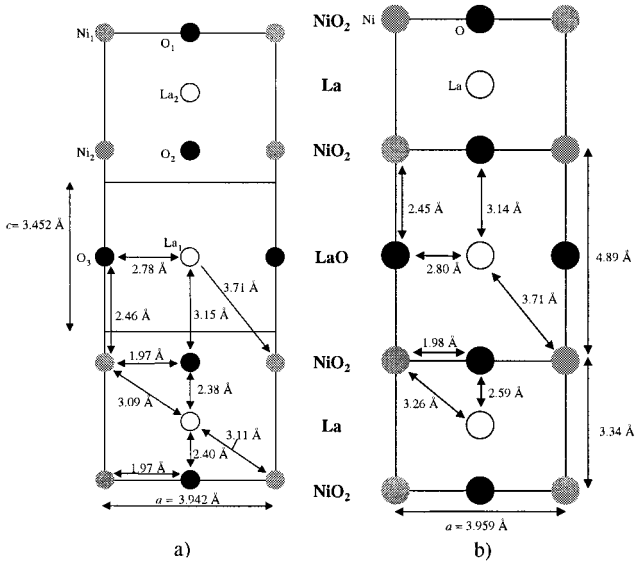

Figure 9. (a) Local structure and bond lengths in the region around a defect NiO_2−LaO−NiO_2 stacking unit in the minority defect phase, interpreted from the positions in lamellar $LaNiO_{2+x}$ refined from neutron powder diffraction data. (b) Local structure and bond lengths in the vicinity of the NiO_2−LaO−NiO_2 defect layers as described within the DIFFaX simulation model.

different stacking sequences (NiO_2−La−NiO_2 and NiO_2−LaO−NiO_2, respectively, see Figure 10) observed in the minority, $LaNiO_{2.09}$, defect phase refined from the neutron diffraction data.

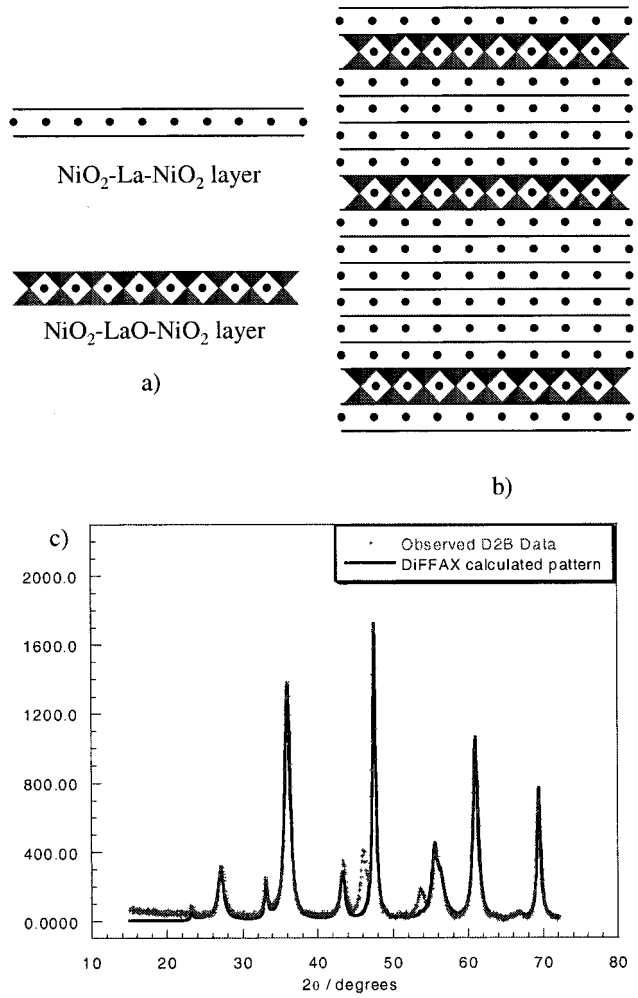

Figure 10. (a) NiO_2−La−NiO_2 and NiO_2−LaO−NiO_2 stacking sequences used in the DIFFaX program to simulate diffraction patterns of the defect structure of $LaNiO_{2.03}$. (b) Example of a faulted crystal formed by stacking NiO_2−La−NiO_2 units with NiO_2−LaO−NiO_2 units using the probabilities defined in Table 3. (c) Neutron powder diffraction pattern of $LaNiO_{2.03}$ calculated using the DIFFaX program, employing the model in Table 3, compared with the observed D2B data. The unfitted Bragg reflections are from the Ni metal impurity.

Describing the structure by the probabilistic stacking of these layers directs information about transitions between NiO_2−La−NiO_2 and NiO_2−LaO−NiO_2 stacking units and the associated relaxation of the NiO_2−La−NiO_2 matrix, as shown in Figure 9b. The description of the minority phase is enhanced by the inclusion of "stacking uncertainty" factors for layer 2, introducing an ellipsoidal error spread for the translation vector, $\mathbf{R}_{ij}$, to allow for the effect of internal strain arising from the insertion of a defect NiO_2−LaO−NiO_2 stacking unit and the resulting perturbation of the surrounding NiO_2−LaO−NiO_2 over a number of unit cell lengths.

Localization of interlamellar defects within discrete layers improves the agreement between the calculated and observed patterns significantly. With randomly distributed defects the number of NiO_2−LaO_{1-x}−NiO_2 stacking units required in the model, to achieve the experimentally measured stoichiometry, is much greater, resulting in a much broader peak shape than observed. It should be noted that the transition probability α_{33} is zero, maintaining the five-coordinate environment around Ni_2 refined from the data (increasing α_{33} above 0.03 resulted in significant intensity mismatches between the simulated and observed diffraction patterns). The powder neutron diffraction

Table 3. Description of Stacking Units and Transition Probabilities Employed in the DIFFaX Simulations of Defect Structure of $LaNiO_{2.03}$

Layer 1

atom	*x*	*y*	*z*
Ni	0	0	0
La	0.5	0.5	0.5
O	0.5	0	0
O	0	0.5	0

i,*j*	α_{ij}	$\mathbf{R}_{ij}$		
1,1	0.75	0	0	1
1,2	0.25	0	0	1
1,3	0			

mole fraction of layer 70.2%

Layer 2

atom	*x*	*y*	*z*
Ni	0	0	0
La	0.5	0.5	0.51
O	0.5	0	0
O	0	0.5	0

i,*j*	α_{ij}	$\mathbf{R}_{ij}$			B_{11}	B_{22}	B_{33}
2,1	0.65	0	0	1.02	0	0	2
2,2	0.25	0	0	1.02	0	0	2
2,3	0.1	0	0	1.02	0	0	2

mole fraction of layer 27.02%

Layer 3

atom	*x*	*y*	*z*
Ni	0	0	0
La	0.5	0.5	0.725
O	0.5	0	0
O	0	0.5	0

i,*j*	α_{ij}	$\mathbf{R}_{ij}$		
3,1	0			
3,2	1	0	0	0.145
3,3	0			

mole fraction of layer 2.7%

[a] Atomic positions and translation vectors are defined relative to the basis lattice parameters: $a = b = 3.959$ Å, $c = 3.373$ Å. Uncertainty factors (B_{11}, B_{22}, B_{33}) define an error spread for the translation vector $\mathbf{R}_{ij}$ in an analogous manner to the way in which Debye−Waller factors describe the uncertainty in atomic position due to thermal motion. The values quoted for the uncertainty factors are related to the rms displacement of the layers, U_{ij}, by $\mathbf{R}_{ij} = 2\pi^2 a_i^* a_j^* U_{ij}$.

pattern simulated using this model can be seen to be in good agreement with the observed data, as shown in Figure 10c.

The average composition of the lanthanum nickelate phases derived from the Rietveld refinement of the powder neutron data is $LaNiO_{2.025\pm0.003}$. The thermogravimetric data, detailed in Figure S2 (Supporting Information) for the reoxidation of $LaNiO_{2+x}$ with oxygen, along with a value of 5.66% Ni metal by mass in the sample (obtained from the Rietveld refinement of the powder neutron data; see Table 2), give an average composition of $LaNiO_{2.11\pm0.02}$.

The apparent disparity between refined and thermogravimetrically measured stoichiometries can be partially accounted for by the observed air sensitivity of $LaNiO_{2+x}$.

Thermogravimetric analysis of the new infinite-layer phase $NdNiO_{2+x}$ is limited to the statement that the minimum value of *x* is 0.04 due to the lack of accurate quantification of the impurities present in these samples (any unaccounted for Ni metal, and accompanying Nd_2O_3 present, will make *x* appear smaller than its true value).

Magnetic Characterization. The analysis of the magnetic properties of $LaNiO_2$ has been hampered by small amounts of ferromagnetic nickel impurities masking the behavior of the bulk sample. Magnetic measurements on six different samples of $LaNiO_2$ show the figure of 5.66% Ni metal by mass for the bulk powder neutron diffraction sample above is by far the largest observed for any sample measured. A more typical figure of between 1.5 and 2% is observed for most samples. As noted above samples reduced from "high pressure" $LaNiO_3$ contain smaller amounts of nickel metal impurities. The size of sample reduced appears to have no direct bearing on the amount of Ni produced. However, maintaining the reaction temperature below 200 °C does reduce the amount of nickel impurity within samples (500 mg aliquots of the same "high pressure" $LaNiO_3$ sample reduced for 3×3 days at 180 and 205 °C, respectively, had 1.8% and 2.6% Ni by mass).

Therefore, magnetic measurements were performed on "high pressure" samples, which were reduced, as described above, at 190 °C, to further minimize the amount of metallic nickel impurity.

Powder neutron diffraction data collected at room temperature on the D2B instrument at the Institut Laue Langevin, Grenoble, France, were readily refined, as described above, without the introduction of any ordered magnetic contribution to the scattering of the lanthanum nickelate phases. Data were also collected at 5 and 300 K on the D1B instrument, and neither data set displayed any features which could not be modeled well on the basis of nuclear scattering alone. Any attempt to introduce ferromagnetic ordering models resulted in the magnitude of the ordered moment refining to zero in both lamellar phases.

Similarly, the introduction of antiferromagnetic ordering models, such as that displayed by $Ca_{0.85}Sr_{0.15}CuO_2$ (antiferromagnetically ordered sheets of CuO_2 aligned such that interactions between adjacent sheets are also antiferromagnetic), yielded no ordered magnetic moment in the lanthanum nickelate phases (the largest ordered moment consistent with the 5 K neutron diffraction data is 0.05 μ_B per nickel atom).

Measurement of the magnetic behavior of the bulk material was performed by measuring magnetization isotherms at a range of temperatures and then using the subtraction method described in the Experimental Section. It should be noted that this procedure is only valid if the nickel metal particles present in the sample are ferromagnetic rather than superparamagnetic. The average particle size estimated from the Rietveld profile refinement (see Table S1 in the Supporting Information) would appear to suggest that the nickel particle size is considerably larger than that expected for a superparamagnet (for a blocking temperature of 300 K the critical radius is on the order of 40 Å[36]), so the procedure in this case is valid. It should, however, be noted that a wide range of nickel particle sizes may be present in the sample, some potentially below 40 Å in radius; therefore, the values of the paramagnetic susceptibility derived by this method should be regarded as an upper limit for the bulk $LaNiO_{2.03}$ phase. Figure 11i shows a typical linear fit to a series of isothermal magnetization measurements, the slope of which is the paramagnetic susceptibility of the nonferromagnetically saturated material in the sample. Figure 11ii shows the plot of the fitted molar susceptibility measured by the subtraction procedure plotted against temperature, for $LaNiO_2$.

The paramagnetic susceptibility appears to be largely temperature independent (rising by only 60% from 300 to 4 K)

(36) Morrish, A., H, *The Physical Principles of Magnetism*, 1st ed.; Wiley: New York, 1965; p 362.

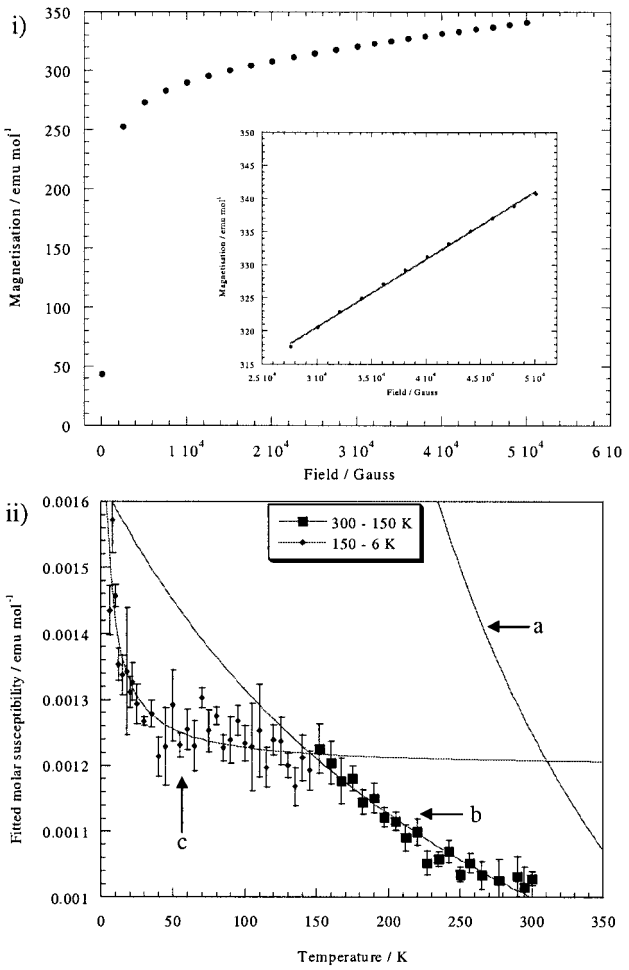

Figure 11. (i) Magnetization-field isotherm of $LaNiO_{2+x}$ at 300 K. The inset shows the linear fit to the high-field data. $\chi_{paramagnetic} = [1.013(9)] \times 10^{-3}$ emu mol^{-1}, intercept (saturated ferromagnetic magnetization) 290.3(3) emu mol^{-1}, goodness of fit $R = 0.9989$. (ii) Fitted molar paramagnetic susceptibility of $LaNiO_2$. The data are shown as squares and diamonds in the temperature ranges $300 > T/K > 150$ and $150 > T/K > 6$, respectively. Curve fits: (a) Curie susceptibility ($\Theta = 0$ K) for an $S = {}^1/_2$ spin-only paramagnet; (b) Curie−Weiss + temperature-independent term ($C/(T - \Theta) + \alpha$), $S = {}^1/_2$, $\Theta = -257$ K, $\alpha = 3.7 \times 10^{-4}$ emu mol^{-1}, $R = 0.97$; (c) Curie−Weiss + temperature-independent term ($C/(T - \Theta) + \alpha$), $C = 0.0031$ (corresponding to ~1 mol % $S = {}^1/_2$ spins), $\Theta = -4$ K, $\alpha = 0.0012$ emu mol^{-1}, $R = 0.94$.

and is significantly smaller than would be expected for an $S = {}^1/_2$ noninteracting paramagnet (which is indicated by curve a in the figure). The small temperature dependence confirms our assertion that the small particles of nickel, observed in the powder neutron diffraction data, are behaving ferromagnetically rather than superparamagnetically, as any superparamagnetic contribution to the fitted susceptibility (which would not have been removed by the subtraction) would display a strong temperature dependence.[37]

The susceptibility data are best described by considering two temperature regions; $6 < T/K < 150$ and $150 < T/K < 300$. At high temperatures, $150 < T/K < 300$, the susceptibility gives a reasonable fit to the sum of a temperature independent term and a Curie−Weiss paramagnetic term with S set equal to ${}^1/_2$ (curve b). The Weiss constant is very large and negative (−257 K), indicating significant correlation between spins and departure from strict Curie−Weiss behavior. The susceptibility then reaches a plateau over the region $50 < T/K < 150$ before climbing again from 50 to 6 K. This temperature range can be again be modeled by the sum of Curie−Weiss and temperature independent terms (curve c). In this low temperature range the temperature-independent term dominates the paramagnetic susceptibility with only a few (~1 mol %) weakly antiferromagnetically coupled spins ($\Theta = -4$ K) remaining.

The measured resistivity of the sample is 10(±5) Ω cm at 300 K (the metallic phases $LaNiO_3$ and $NdNiO_3$ have resistivities on the order of 5×10^{-3} Ω cm at 300 K[38]). It should be noted, however, that this value of the resistivity is only an estimate and may be heavily influenced by contact effects and the presence of metallic nickel particles.

Discussion

Sodium hydride can effect the topotactic reduction of $LaNiO_3$ to $LaNiO_2$, which is not possible with flowing hydrogen or metal getter reagents. The large reduction potential of the H^- ion, in NaH,[22] has allowed the isolation of $LaNiO_2$ at a temperature below 210 °C, where most other reducing agents would not be effective. The difficulties experienced in preparing this material with other reagents may be attributed to its low thermal stability—$LaNiO_2$ disproportionates into $La_2Ni_2O_5$, La_2O_3, and Ni on annealing above 210 °C under vacuum (this is in contrast with the only previous report of the reduction of $LaNiO_3$ to $LaNiO_2$ "below 670 K" in a recirculating hydrogen/helium system by Crespin et al.[10,11]). This lack of thermal stability may also be the reason stoichiometric $LaNiO_2$ is not synthesized by this method. As reaction temperatures approach 210 °C, there may be kinetic competition between reduction and decomposition, preventing reaction completion.

Determination of the exact mechanism by which NaH is reducing $LaNiO_3$, below 210 °C, will require further research, but it does not appear to involve hydrogen or oxygen gas as intermediates. There are three major mechanisms that could be operating in the reduction reaction:

$$2NaH(s) + LaNiO_3(s) \rightarrow 2Na(s) + \mathbf{H_2(g)} + LaNiO_3(s) \rightarrow 2Na(s) + H_2O(g) + LaNiO_2(s) \rightarrow NaOH(s) + NaH(s) + LaNiO_2(s) \quad \text{(a)}$$

$$NaH(s) + LaNiO_3(s) \rightarrow NaH(s) + LaNiO_2(s) + {}^1/_2\mathbf{O_2(g)} \rightarrow NaOH(s) + LaNiO_2(s) \quad \text{(b)}$$

$$NaH(s) + LaNiO_3(s) \rightarrow NaOH(s) + LaNiO_2(s) \quad \text{(c)}$$

Note that these equations are only intended to distinguish solid−solid from solid−gas mechanisms and therefore do not explicitly contain the $La_2Ni_2O_5$ intermediate seen experimentally.

Martinez-Lope et al.[39] reported that $LaNiO_3$ is stable up to a temperature of 250 °C in a 5%/95% H_2/N_2 atmosphere, in agreement with our observation that $LaNiO_3$ did not undergo any significant reduction, on a thermogravimetric balance, after 10 h at 200 °C in a 5%/95% H_2/N_2 atmosphere. Reduction to $La_2Ni_2O_5$ occurs, with intimately mixed NaH, in the temperature range $120 < T/°C < 180$. Reaction of physically separated $LaNiO_3$ and NaH, within an evacuated Pyrex tube, results in no observable reaction below 220 °C. This evidence would appear to discount both mechanisms a and b, which have gaseous reaction intermediates and therefore do not require

(37) Leslie-Pelecky, D. L.; Rieke, R. D. *Chem. Mater.* **1996**, *8*, 197.

(38) Blasco, J.; Castro, M.; Garcia, J. *J. Phys.: Condens. Matter* **1994**, *6*, 5875−5889.

(39) Martinez-Lope, M. J.; Alonso, J. A. *Eur. J. Inorg. Chem.* **1995**, *32*, 361.

physical contact between reagents. Reduction of $LaNiO_3$ to $La_2Ni_2O_5$ did occur above 220 °C, when the reagents were physically separated, presumably via mechanism a (decomposition of NaH to Na and H_2), as the decomposition temperature of NaH is 210 °C (defined as the temperature required to produce a hydrogen pressure of 10 mmHg[40]) and getter reactions similar to mechanism b do not occur until much higher temperatures (reaction between $LaNiO_3$ and a Zr getter requires a temperature of at least 400 °C[4]). The products obtained by the use of physically separate NaH, at temperatures where a significant H_2 partial pressure is present, agree well with those found using H_2(g).

Additional evidence to suggest mechanism c (diffusion between solids) is occurring with the intimately mixed reagents is provided by the observation that the rate of reaction is affected by the sample size (large samples react more slowly), mixing of reagents (poorly mixed samples react more slowly), and ratio of NaH to $LaNiO_3$ (increasing the amount of NaH with respect to $LaNiO_3$ increases the reaction rate at a given temperature).

All three observations indicate physical contact between the reagents is required for reaction, suggesting the reduction occurs via diffusion between solids (c) rather than via a gaseous intermediate (a, b). The key point is that $LaNiO_2$ is not formed by either route (flowing H_2 or separated reagents within a sealed tube) involving gas-phase hydrogen as a reducing agent.

Analysis of neutron powder diffraction and high-resolution electron microscopy data has shown that $LaNiO_{2+x}$ has a defect microstructure which requires a significant modification of the infinite-layer model, proposed by Crespin et al., in a manner not previously observed in the defect chemistry of infinite-layer cuprates.

The refined structure consists of two tetragonal phases with similar *a* lattice parameters but significantly different *c* lattice parameters due to the incorporation of interlamellar oxide ion defects. The first is a highly ordered phase which has the "perfect" infinite-layer structure and is observed to exist in crystalline domains which have far larger dimensions in the *ab* plane of the material than in a direction parallel to the stacking direction (*c* axis) (Table S1).

At first sight, the Ni^I-O bond lengths for the majority phase (1.979 Å) are among the longest reported for Ni^I in the solid state. However, it should be noted that there are very few examples suitable for direct comparison with the infinite sheets found here, as most reported Ni^I oxides display either strikingly different coordinations, for example the linear NiO_2 units in $(K,Rb)Na_2NiO_2$ (Ni−O = 1.77 Å[41]), or significant disorder in the nickel coordination shell, e.g. $LaSrNiO_{3.1}$[42] or the $LnSr_5Ni_3O_8$ phases.[5] When only the Ni^I-O distances to fully ordered oxygen sites are considered, the refined bond length for the stoichiometric $LaNiO_2$ appears to be reasonable (the nondisordered Ni^I-O bond length in $LaSrNiO_{3.1}$ is 2.04 Å;[42] nondisordered Ni^I-O bond lengths in $LnSr_5Ni_3O_8$ range from 1.995(7) Å for Ln = Ho to 1.986(7) Å for Ln = Y[5]).

The second tetragonal phase deviates significantly from the "perfect" infinite-layer model, exhibiting disordering of the NiO_2 planes driven by the presence of additional interlamellar oxide ions which change the average stoichiometry of the phase to $LaNiO_{2.09(1)}$. Closer inspection shows that the disorder in this phase can be more accurately viewed as the superposition of two different substructures, the "perfect" infinite-layer model (exhibiting $NiO_2-La-NiO_2-La$ stacking) and a defect phase (exhibiting defective layers of $NiO_2-LaO-NiO_2$). The superposition observed in the second phase models regions of the sample where the two stacking sequences have intergrown intimately with each other, as shown in Figure 10. That is to say, the minority phase consists of defective $NiO_2-LaO-NiO_2$ blocks inserted within a relaxed $NiO_2-La-NiO_2-La$ stacking sequence.

The strain parallel to the stacking direction is over 4 times that observed parallel to the NiO_2 planes in the minority phase, due to the significant mismatch in the *c* lattice parameters (stacking repeat length) between the intergrowing sequences ((*c*-defect(Ni−O−Ni)/*c*-perfect(Ni-vacancy-Ni) = 1.46), which results in a considerable strain in the stacking direction, compared to the small strain within the NiO_2 planes ((*a*-defect/*a*-perfect) = 0.996). The combination of both anisotropic particle size and uniaxial strain leads to the highly anisotropic diffraction peak widths observed for this phase.

The coordination around nickel in the minority phase must be discussed in terms of two sites. (a) Site Ni_1, the majority (62.3%) of the nickel atoms in this phase occupy this site and exhibit square-planar coordination with bond lengths very similar to those of the majority phase (1.972 Å as opposed to 1.979 Å in the majority phase). (b) Site Ni_2, a disordered site displaced due to its proximity to an interlamellar oxide ion (O_3). The Ni_2 position has four in-plane oxygen contacts (Ni_2-O_2) of 1.972 Å, and the symmetry of the *P*4/*mmm* space group also generates two Ni_2-O_3 bond lengths (1.00 and 2.46 Å). However, Ni(I) would be expected to exhibit a large Jahn−Teller distortion (cf. La_2CuO_4); therefore, all Ni_2-O_3 bond lengths should be considerably in excess of 1.979 Å. The shorter Ni_2-O_3 bond length is thus rejected as unphysical, reinforcing the picture of the minority phase as the superposition of two constituent phases, as shown in Figures 8 and 9. Ni_2 thus adopts square-pyramidal coordination, consistent with a large Jahn−Teller distortion at Ni(I). The ratio $Ni-O_{axial}/Ni-O_{equatorial}$ (Ni_2-O_2/Ni_2-O_3) refined for the minority lanthanum nickelate phase is 1.247, which compares well with a value of 1.289 for La_2CuO_4 (four- plus two-coordination)[43] and an average value of 1.202 for the Cu−O bond lengths in $YBa_2Cu_3O_{7-x}$ (square-pyramidal coordination).[44] All interatomic contacts to O_3 should be viewed in the light of the large rms displacement of this ion (0.28 Å). The defective regions, therefore, correspond to the insertion of vertex-linked NiO_5 square pyramids into the stacking sequence.

By analysis of the other metal−oxygen bond lengths (La_1-O_2 for example) and rejection of the physically unreasonable short contacts, it becomes clear that a model of the local structure around a defect $NiO_2-LaO-NiO_2$ block can be constructed, from the refined minority phase, as shown in Figure 9a. The apparent compression of the $NiO_2-La-NiO_2$ blocks directly adjacent to the defect layer is exaggerated in this scheme, however, due to the imposition of a common *c* lattice parameter onto the intergrowth of the two stacking units. The refined positions of the NiO_2 layers, constructed from Ni_1 and O_1, should therefore be considered a weighted average of positions summed over the locally relaxed $NiO_2-La-NiO_2$ matrix. Evidence for this can be seen in the large displacement factors associated with Ni_1 and O_1. The rms displacements of

(40) Greenwood, N. N.; Earnshaw, A. *Chemistry of the Elements*, 2nd ed.; Butterworth-Heinemann: Oxford, U.K., 1997; p 66.
(41) Burow, W.; Birx, J.; Bernhardt, F.; Hoppe, R. *Z. Anorg. Allg. Chem.* **1993**, *619*, 923.
(42) Crespin, M.; Landron, C.; Odier, P.; Bassat, J. M.; Mouron, P.; Choisnet, J. *J. Solid State Chem.* **1992**, *100*, 281.
(43) Longo, J. M.; Raccah, P. H. *J. Solid State Chem.* **1973**, *414*, 526.
(44) David, W. I. F.; Harrison, W. T. A.; Gunn, J. M. F.; Moze, O.; Soper, A. K.; Day, P.; Jorgensen, J. D.; Hinks, D. G.; Beno, M. A.; Soderholm, L.; Capone, D. W.; Schuller, I. K.; Segre, C. U.; Zhang, K.; Grace, J. D. *Nature* **1987**, *327*, 310.

the ions (0.28 and 0.24 Å, respectively) are large enough to extend the short La−O and La−Ni bonds described in Figure 9a to the more physical values used in the DIFFaX model and shown in Figure 9b.

It should be noted that the $O_3-Ni_2-O_3$ angle, in the disordered phase, is 179.7(2)°, indicating the NiO_2 sheets are very nearly planar. This implies that the NiO_2 sheets have been separated by the insertion of oxygen at (0, 0, $^1/_2$) with very little buckling, providing further evidence that the interlamellar oxide ions are localized in distinct layers rather than distributed randomly throughout the whole lattice.

The magnetic data show that all samples are contaminated by small amounts of metallic nickel. This has been assigned to the presence of amorphous NiO in the $LaNiO_3$ starting material, which could not be observed by powder X-ray diffraction but which is readily reduced to Ni metal by NaH. The significantly smaller amounts of nickel metal in samples reduced from "high pressure" $LaNiO_3$ would appear to confirm this. Measurement of the magnetic behavior of the bulk sample provides no evidence for any long-range magnetic order in $LaNiO_2$. The paramagnetic susceptibility of this Ni(I) phase, measured by the subtraction of the ferromagnetic impurity signal, appears to be largely temperature independent, with a value considerably less than that expected for an ideal $S = {}^1/_2$ spin-only paramagnet. This value of the susceptibility must be considered as an upper limit on that of bulk $LaNiO_{2.03}$, in view of the possible complications from superparamagnetic nickel particles, and thus implies that the two-dimensional NiO_2 sheets are not simply layers of uncoupled $S = {}^1/_2$ spins. One possible interpretation of the small temperature dependence of the paramagnetic susceptibility is that $LaNiO_{2.03}$ is metallic. The measured resistivity is, however, several orders of magnitude higher than is usually found for metallic oxides. A model of strongly antiferromagnetically coupled localized $S = {}^1/_2$ centers is thus preferable, although the nature of the transition between regions b and c in Figure 11ii, at 150 K, remains to be clarified, as neutron powder diffraction data indicate the absence of long-range magnetic order in $LaNiO_{2.03}$.

The electronic properties are in contrast with those of undoped Cu(II) oxides, which are universally found to be antiferromagnetically ordered. The absence of such long-range order here, unambiguously shown by neutron powder diffraction, has two possible causes. The slight oxidation beyond Ni(I) in the defective regions of the structure may introduce sufficient carriers to suppress ordering (only 3% of Cu(III) centers are required to totally suppress antiferromagnetic order in $La_{2-x}Sr_xCuO_4$ [45]) throughout the bulk phase. Alternatively, the reduced covalency between the Ni 3d and O 2p orbitals in the nickelates significantly reduces the strong antiferromagnetic superexchange associated with the close Cu 3d−O 2p energy match in the cuprates. The large Weiss constants and significant temperature-independent terms required to model the paramagnetic susceptibility suggest that this strong spin−spin coupling is retained, however, and that the observed behavior results from suppression of long-range order by the d^8 centers introduced on partial oxidation. The preferred interpretation of the neutron and spin susceptibility data is that strong antiferromagnetic coupling between the $S = {}^1/_2$ centers gives rise to a transition to a short-ranged ordered or frozen state below 150 K, three-dimensional ordering being suppressed by the structural and electronic effects of the interlamellar oxide ions.

The tetragonal phase, $NdNiO_{2+x}$, synthesized via the reduction of $NdNiO_3$ with NaH, is expected to have a defect structure similar to that of $LaNiO_2$ due to the highly anisotropically broadened reflections seen in all X-ray powder diffraction patterns of this phase and the stoichiometry measured by thermogravimetric analysis. The lattice parameters ($a = 3.9251(9)$ Å, $c = 3.323(1)$ Å, $V = 51.195$ Å^3) of this phase in comparison with those derived from a single-phase model of $LaNiO_2$ ($a = 3.961$ Å, $c = 3.381$ Å, $V = 53.046$ Å^2) are consistent with the reduction in ionic radius from La^{3+} to Nd^{3+}. The thermal stability of $NdNiO_{2+x}$ mirrors that of $LaNiO_{2+x}$, with disproportionation into poorly crystalline products occurring above 200 °C (the only phase identifiable from powder X-ray diffraction was Nd_2O_3).

Conclusion

Sodium hydride affords the metastable Ni(I) oxide $LaNiO_2$ in a solid-state metathesis[46] reduction reaction, allowing characterization of the (defect) structure and electronic properties of this phase. The predominantly lamellar structure is interrupted by defective regions where interlamellar oxide anions aggregate, producing five-coordinate metal centers. Electronically, the d^9 Ni(I) two-dimensional sheets appear to behave quite differently from their isoelectronic Cu(II) counterparts, with no antiferromagnetic long-range order, despite evidence that the $S = {}^1/_2$ centers are strongly coupled. Isolation of the metastable lamellar Ni(I) phase is possible because the more powerful NaH(s)/NaOH(s) couple reduces $LaNiO_3$ at lower temperatures than the $H_2(g)/H_2O(l)$ couple. There appears to be no reason the use of solid hydrides cannot be extended to the topotactic reduction of a wide range of solid-state materials. As reagents they are easy to handle and readily available, giving access to materials which cannot be synthesized by existing routes. In this specific instance the low decomposition temperature of NaH (210 °C) limits its use, as above this temperature a significant pressure of hydrogen is present, potentially preventing the formation of highly metastable intermediates. There are, however, a range of other solid hydrides with much higher decomposition temperatures (LiH, ∼550 °C; CaH_2, ∼885 °C[40]) which could be readily employed to perform solid-state reductions over a wide temperature range.

Acknowledgment. We thank the donors of the Petroleum Research Foundation, administered by the American Chemical Society, and the EPSRC for support of this work. We thank Dr. P. G. Radaelli for his expert assistance with the collection of powder neutron diffraction data at the Institut Laue Langevin, Grenoble, France.

Supporting Information Available: Figure S1, a Rietveld profile refinement for the "single phase" fit to the neutron powder diffraction data, Figure S2, thermogravimetric and differential scanning calorimetric plots for the reoxidation of $LaNiO_{2+x}$, and Table S1, strain and particle sizes evaluated from the refined profile coefficients of the two-phase fit to the neutron powder diffraction data. This material is available free of charge via the Internet at http://pubs.acs.org.

JA991573I

(45) Budnick, J. T.; Chamberland, B.; Yang, D. P.; Niedermayer, C.; Golnik, A.; Recknagel, E.; Rossmanith, M.; Weidinger, A. *Europhys. Lett.* **1988**, *5*, 651−656.

(46) Treece, R. E.; Gillan, E. G.; Kaner, R. B. *Comments Inorg. Chem.* **1995**, *16*, 313.